Article

Spatiotemporal Changes in and Driving Factors of Potential Evapotranspiration in a Hyper-Arid Locale in the Hami Region, China

Yuanbo Lu [1,2,3], Lingxiao Sun [1], Chunlan Li [1], Jing He [1], Zengkun Guo [1,2,3], Li Duan [1,2,3], Jing Zhang [1,2,3], Ewa Łupikasza [4], Ireneusz Malik [4], Małgorzata Wistuba [4] and Yang Yu [1,2,*]

1   Key Laboratory of Ecological Safety and Sustainable Development in Arid Lands, Xinjiang Institute of Ecology and Geography, Chinese Academy of Sciences, Urumqi 830011, China; hejing@ms.xjb.ac.cn (J.H.)
2   State Key Laboratory of Desert and Oasis Ecology, Xinjiang Institute of Ecology and Geography, Chinese Academy of Sciences, Urumqi 830011, China
3   College of Resources and Environment, University of Chinese Academy of Sciences, Beijing 100049, China
4   Faculty of Earth Sciences, University of Silesia in Katowice, 41-200 Sosnowiec, Poland; ewa.lupikasza@us.edu.pl (E.Ł.); irekgeo@wp.pl (I.M.); malgorzata.wistuba@us.edu.pl (M.W.)
*   Correspondence: yuyang@ms.xjb.ac.cn

Abstract: Potential evapotranspiration (*PET*) is a crucial variable for implementing adaptation measures to mitigate the potential impacts of climate change on water resources. In the context of global warming, *PET* is essential for predicting water resource supply and demand, guiding irrigation and water management decisions. However, there is limited understanding of the spatiotemporal changes in *PET* and its driving factors in the hyper-arid regions of Northwest China. In this study, the Hargreaves model was employed to estimate *PET* in the Hami region from 1991 to 2020. By combining relevant climate data and partial correlation analysis, we investigated the spatiotemporal distribution patterns of *PET* within the study area and analyzed the factors influencing these patterns. The results showed the following: (1) From 1991 to 2020, the overall *PET* in the Hami region demonstrated a tendency to rise. The interannual trend rates of *PET* for the full year, spring, summer, autumn, and winter were 0.933, 2.744, 0.906, 0.488, and −0.406 mm·a-1, respectively. Despite a decreasing trend in winter *PET*, the other seasonal *PET* values and the annual *PET* values exhibited an increasing trend. (2) The spatial distribution of both annual and seasonal *PET* showed significant regional heterogeneity, following a consistent pattern marked by lower values in the central part and higher values in the surrounding areas. The southern region tended to have relatively high *PET*, while the northwestern region experienced comparatively low *PET*. (3) Partial correlation analysis indicated significant differences in the impact of various climatic factors on *PET*. The maximum temperature emerged as the dominant factor influencing annual *PET* variation, while precipitation played a leading role in influencing autumn *PET* variation. This study underscores the influence of climate change on *PET* in the Hami region, contributing to an enhanced comprehension of *PET* variations.

Keywords: potential evapotranspiration; Hargreaves model; driving factors; hyper-arid; climate change; Hami region

1. Introduction

Evapotranspiration (*ET*) is a physical process intricately linked to the atmosphere, vegetation, soil, and human activities, directly shaping surface water cycling and energy balance and profoundly influencing water availability [1,2]. It plays a crucial role in the estimation and management of agricultural water demand [3]. Potential evapotranspiration (*PET*) represents the highest potential amount of water loss through evapotranspiration, serving as a crucial element in regional and global Earth system dynamics [4,5]. *PET* not only serves as the basis for calculating actual evapotranspiration but also constitutes an

indispensable input for several important conceptual models. These include the Palmer Drought Severity Index (PDSI) [6], the aridity index (AI) [7] and hydrological models [8,9]. Therefore, gaining a comprehensive understanding of the dynamic processes of potential evapotranspiration (*PET*) and its influencing factors against the backdrop of climate change is of paramount significance. Such insights contribute to advancing regional and global hydrological and ecological research in addition to fostering sustainable societal development.

The application fields of *PET* are diverse, and there are various calculation models available. Examples include the Penman-Monteith (PM) model [10], which has been made accessible by the Food and Agriculture Organization of the United Nations (FAO); the Hargreaves model [11]; and the Priestley-Taylor model [12], among others. The numerous calculation models for *PET* indicate that there are numerous influencing factors, and the causes of variations are highly complex [13,14]. In addition to meteorological driving factors such as wind speed, temperature, vapor pressure deficit, and solar radiation, the structural, compositional, and distributional changes in plant communities also play a crucial role in the evolution of *PET* [15,16]. Currently, research on the impact of vegetation on *PET* is relatively limited [17]. Most studies have focused predominantly on the influence of climate change on *PET* [18–20]. However, there are significant variations in the factors influencing *PET* changes across different regions. Some studies suggest that a decrease in solar radiation is the reason for reduced *PET* in China and the United States [21,22]. On the other hand, research on the northeastern part of India [23], the Canadian prairies [24], and large parts of Australia [25] indicates that changes in wind speed are the factors contributing to *PET* reduction. The spatiotemporal heterogeneity of climate change is the fundamental reason for the diverse outcomes observed. Therefore, further in-depth research is needed to understand the regional variations in *PET* and its controlling factors.

The Hami region is situated in the eastern part of Xinjiang, China, and represents a typical arid area characterized by a dry climate and limited water resources. Agriculture, water resource management, and ecological balance face unique challenges in this region. In recent years, with the increasingly significant impact of climate change, the hydrological processes and dynamic changes in ecosystems in the Hami region have garnered widespread attention. A thorough understanding of the interactions among hydrological cycles, vegetation dynamics, and climate change in this region would contribute to filling knowledge gaps in water resource management and climate adaptation in arid areas. This knowledge forms the scientific groundwork for the region's sustainable development.

The study of *PET* in the Hami region holds profound significance. *PET*, as a crucial parameter in the water cycle, plays a vital role in the scientific understanding of the distribution of water resources, supply–demand relationships, and the stability of hydroecosystems in the research area. By conducting in-depth research on *PET*, it becomes possible to more accurately predict the availability of water resources and formulate effective water resource management strategies [26]. In addition, in terms of agricultural production, *PET* is directly related to the water needs of plants. By gaining a deeper understanding of *PET*, we can optimize irrigation plans, improve the efficiency of water resource utilization, and thereby achieve sustainable development of agriculture in arid regions.

2. Study Area and Research Methods

2.1. Study Area

Hami is located in the eastern part of the Xinjiang Uygur Autonomous Region, China (40°49′ N, 93°31′ E). Its geographical location exposes it to the influences of the Central Asian continental climate and topography (Figure 1). The climate in the Hami region is a dry continental climate, characterized by hot, dry summers and cold, dry winters. The annual average temperature is relatively high, but there is significant diurnal temperature variation. These climatic conditions have a significant impact on local ecology and agriculture. Due to the dry climate and geographical location, precipitation is relatively scarce in the Hami region, and surface water sources are limited. This has led to a high degree of dependence on groundwater for irrigation and domestic water needs. However, groundwater resources

are also facing challenges of overextraction and depletion. Due to the unique climate in the Hami region, *PET* is a crucial meteorological indicator. The average *PET* during spring, summer, and autumn significantly influences vegetation growth and water management under the arid climate conditions of Hami. Detailed research on this aspect is crucial for effective water resource management and agricultural planning.
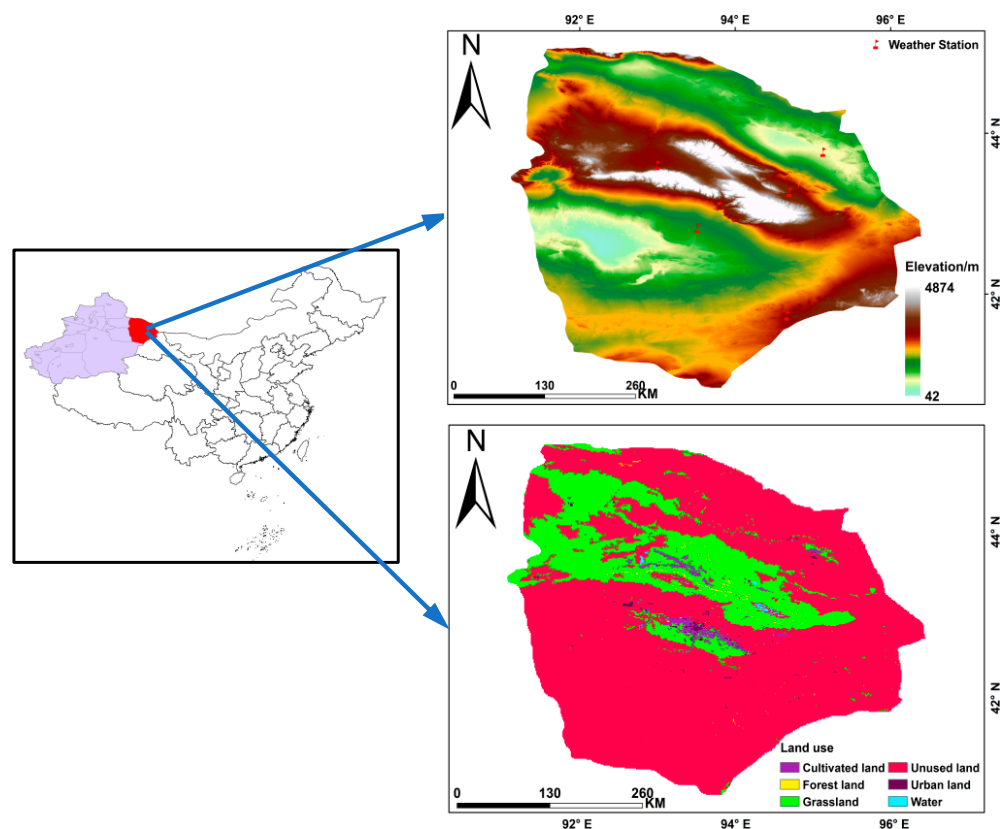

Figure 1. Digital elevation model (DEM) and land-use types of the study area.

2.2. Data Sources

The spatial resolution of precipitation (MAP), average temperature (MAT), maximum temperature (Max-T), and minimum temperature (Min-T) in these datasets was 1 km. The data were generated through spatial downscaling based on the global 0.5° climate dataset released by CRU and the high-resolution global climate dataset released by WorldClim 1.4. The dataset was verified by the publisher using data from 496 weather stations, and the validation results were credible (https://data.tpdc.ac.cn/, accessed on 4 November 2023). The data used in this study ranged from 1991 to 2020. The data for the meteorological station included wind speed (WS), vapor pressure deficit (VPD), sunshine duration (SH), and relative humidity (RH); the details of the data are provided in Table 1. The annual data statistics followed the calendar-year algorithm, summing the values for each month from January to December. Seasonal data were calculated based on the following divisions: March, April, and May constitute spring (SP); June, July, and August constitute summer (SU); September, October, and November constitute autumn (AU); and December to the following February constitute winter (WI).

Table 1. Data Sources and Basic Parameters.

Parameter	Abbreviation	Unit	Original Resolution	Data Source
Mean annual precipitation	MAP	mm	1000 m	https://doi.org/10.5281/zenodo.3185722, accessed on 4 November 2023
Mean annual temperature	MAT	°C	1000 m	https://cstr.cn/18406.11.Meteoro.tpdc.270961, accessed on 4 November 2023
Maximum temperature	Max-T	°C	1000 m	https://doi.org/10.5281/zenodo.3114194, accessed on 4 November 2023
Minimum temperature	Min-T	°C	1000 m	https://doi.org/10.5281/zenodo.3114194, accessed on 4 November 2023
Wind speed	WS	m/s	1000 m	Meteorological station data
Vapor pressure difference	VPD	hpa	1000 m	Meteorological station data
Relative humidity	RH	%	1000 m	Meteorological station data
Sunlight hours	SH	h	1000 m	Meteorological station data

2.3. Research Methods

2.3.1. Hargreaves Model

In the study area, the major land-use type (other than unused land) is grassland; accordingly, the Hargreaves model was used to estimate the process of *PET* under monthly meteorological conditions. The specific expression of the formula is as follows:

$$PET = 0.0023 \times \sqrt{T_{Max} - T_{Min}} \times (T_{Mean} + 17.8) \times S_0 \tag{1}$$

In this formula, *PET* represents potential evapotranspiration (mm/month); T_{Max}, T_{Min}, and T_{Mean} correspond to the monthly maximum temperature, minimum temperature, and mean temperature, respectively; and S_0 is the theoretical amount of solar radiation reaching the top of the Earth's atmosphere.

The calculation of S_0 is typically based on parameters such as the solar constant, Earth–Sun distance, Julian day, and solar declination. The formula is as follows:

$$S_0 = \frac{24 \times 60}{\pi} \times G_s \times \frac{1 + 0.033 \times \cos\left(\frac{2\pi(n-3)}{365}\right)}{\pi \times d^2} \tag{2}$$

In this formula, G_s represents the solar constant, indicating the intensity of solar radiation outside the Earth's atmosphere, approximately 1367 w/m^2; n is the Julian day of the year (1 for 1 January, 365 for 31 December); and d is the Earth–Sun distance, which is the average distance between the Earth and the Sun.

2.3.2. Kriging Interpolation Method

This study employed the Kriging interpolation method to interpolate data for WS, VPD, SH, and RH. The principle of Kriging interpolation involves obtaining the predicted values for specific location points through a specific interpolation calculation formula [27]. The calculation formula is as follows:

$$Z(x_0) = \sum_{i=1}^{n} a_i z(x_i) \tag{3}$$

$$\sum_{i=1}^{n} a_i = 1 \tag{4}$$

In Equations (3) and (4), $Z(x_0)$ is the predicted value of x_0; $z(x_i)$ is the measured value of x_i; and a_i is the weight coefficient of the measured value on the predicted value.

2.3.3. Analysis Methods

Partial correlation analysis is a method used to assess the correlation between two variables while controlling for the influence of a third variable that is concurrently correlated

with both, allowing for a more focused examination of the relationship between the two primary variables. The R value of the correlation coefficient is a decisive factor; a larger R value indicates a stronger correlation between variables, while a lower R value indicates a weaker correlation.

$$R_{ij,k} = \frac{r_{ij} - r_{ik} - r_{jk}}{\sqrt{(1 - r_{ik}^2)(1 - r_{jk}^2)}} \tag{5}$$

where r_{ij} represents the correlation coefficient for a basic correlation between r_i and r_j, r_{ik} represents the correlation coefficient for a basic correlation between r_i and r_k, and r_{jk} represents the correlation coefficient for a basic correlation between r_j and r_k.

The null hypothesis for the partial correlation coefficient test is that the overall partial correlation coefficient between two variables is 0. In the study of *PET*, partial correlation analysis plays a crucial role. Partial correlation analysis allows researchers to more accurately assess the true relationship between *PET* and two variables by considering the influence of other factors; this helps eliminate the interference of external factors, enabling researchers to gain a more precise understanding of the pure correlation between *PET* and a specific meteorological factor. The *t*-test method uses the following formula:

$$T = \frac{R_{ij,k}}{\sqrt{(1 - r_{ij,k}^2)}} \sqrt{(n - m - 1)} \tag{6}$$

In the formula, $R_{ij,k}$ represents the partial correlation coefficient, n is the number of samples, m is the number of independent variables, and (n − m − 1) is the number of degrees of freedom. When ($T < 0.05$ (n − k − 2)) or ($p < 0.05$), the null hypothesis is rejected.

The trends in the variations of each factor are analyzed through linear regression, with each factor as the dependent variable and years as the independent variable. The analysis was used to examine the temporal trends of each factor over the study period.

3. Results and Analysis

3.1. Temporal and Spatial Dynamic Changes in PET

3.1.1. Analysis of Annual Interannual Variation Characteristics in *PET*

The annual and seasonal *PET* variations in the Hami region from 1991 to 2020 are depicted in Figure 2. The trend rate of annual *PET* in Hami was 0.933 mm·a-1 (Figure 2e), indicating an overall increasing trend against the backdrop of global warming. Before 2010, there was significant fluctuation; however, after 2010, the fluctuation amplitude decreased. From a seasonal perspective, the annual trend rates of *PET* for SP, SU, AU, and WI were 2.744, 0.906, 0.488, and −0.406 mm·a-1, respectively (Figure 2a–d). This indicated that, except for WI, in which *PET* showed a declining pattern, all seasons exhibited an increasing trend. Among them, SP showed the most significant increase in *PET*. Additionally, there was a noticeable fluctuation trend in *PET* for each season, with SU and AU showing a similar annual fluctuation pattern.

3.1.2. Analysis of Spatial Variations in *PET*

The regional distribution of annual *PET* in the Hami region from 1991 to 2020 is illustrated in Figure 3. The figure encompasses data for six periods, namely, 1991, 1996, 2001, 2007, 2013, and 2020, depicting the variations in *PET* over these years. Throughout the entire study period, the annual *PET* in the Hami region ranged from 113 to 1111 mm, with a multiyear average of 871.54 mm. The spatial distribution characteristics remained relatively consistent. As can be observed from Figure 3a–f, *PET* exhibited significant regional variations, forming a distribution pattern with lower values in the central part and higher values in the surrounding areas. The southern region, in particular, had the highest *PET* values, while the northwestern region had relatively lower values.

Figure 2. Interannual variation trends of annual and seasonal potential evaporation in Hami region: (**a**) SP average *PET*; (**b**) SU average *PET*; (**c**) AU average *PET*; (**d**) WI average *PET*; (**e**) annual average *PET*).

The regional distribution of *PET* in the Hami region for each season from 1991 to 2020 is illustrated in Figure 4. The figure includes data for the SP, SU, AU, and WI seasons for the years 1991, 2005, and 2020, depicting the variations in *PET* over these three periods. Throughout the entire study period, the spatial distribution of *PET* for each season remained essentially consistent with the annual *PET* pattern. From Figure 4a–l, it can be observed that the average *PET* varied significantly among different seasons. In SP, *PET* ranged from 47 to 1436 mm, with an average of 1052.31 mm calculated over multiple years. For SU, the range was from 309 to 2116 mm, with an average of 1702.61 mm calculated over multiple years. AU exhibited a *PET* range of 77 to 817 mm, with an of 589.82 mm average calculated over multiple years. WI showed a *PET* range of 0 to 261 mm, with an average of 141.93 mm calculated over multiple years. These values represent 30.17%, 48.84%, 16.92%, and 4.07% of the annual *PET*, respectively. Throughout the year, the *PET* followed the order of SU > SP > AU > WI. This trend is consistent with higher values observed in regions characterized by deserts, barren lands, and bare surfaces compared to areas with natural grasslands and orchards.
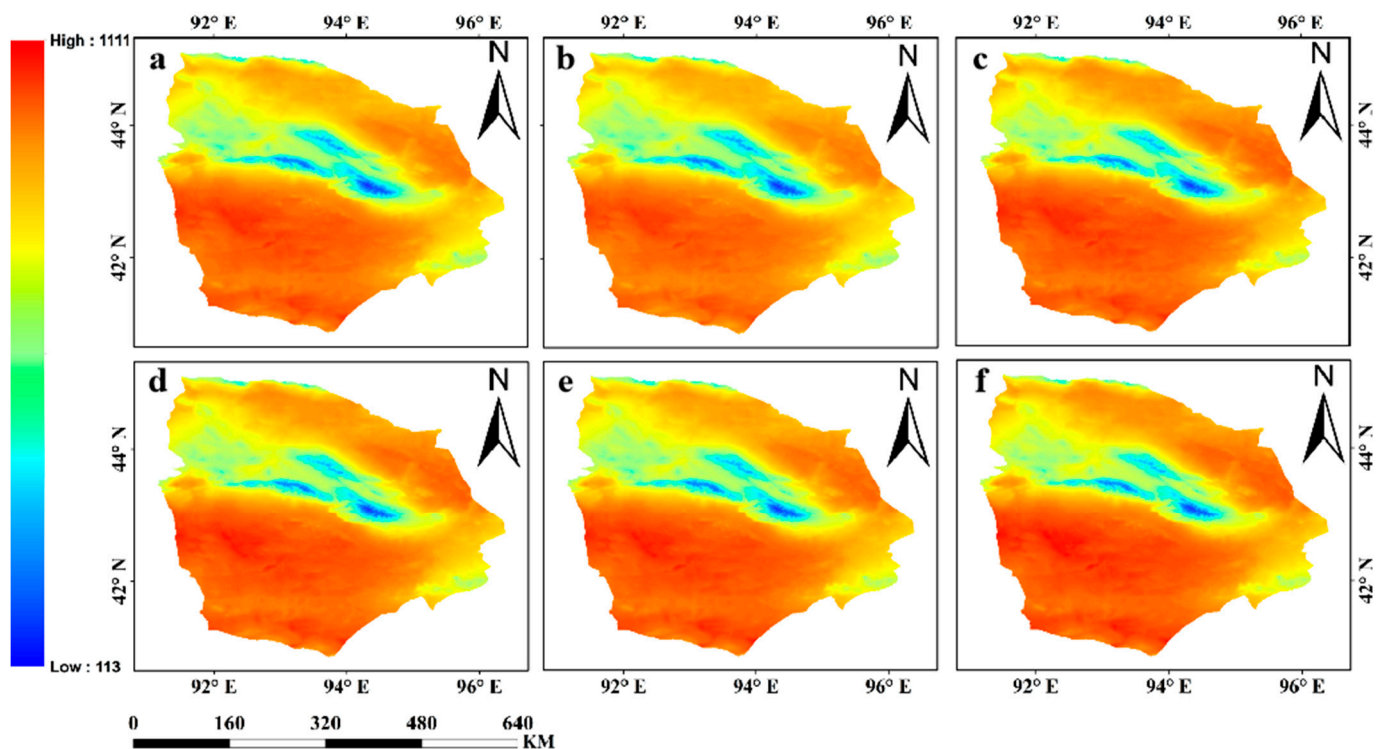
Figure 3. The spatiotemporal distribution of *PET* in the Hami region (**a**–**f**) in 1991, 1996, 2001, 2007, 2013, and 2021 is illustrated. The maps represent the following years: (**a**) 1991; (**b**) 1996; (**c**) 2001; (**d**) 2007; (**e**) 2013; (**f**) 2021.

3.2. Drivers of Spatiotemporal Changes in PET

3.2.1. Spatiotemporal Distribution Characteristics of Environmental Factors in the Hami Region

The temporal and spatial dynamics of various environmental factors in the Hami region from 1991 to 2020 are illustrated in Figures 5 and 6. The multiyear average MAP was 55.79 mm, with a trend rate of -0.18 mm·a-1 (Figure 5a), indicating an overall decreasing trend in MAP in the Hami region. The multiyear average MAP values for SP, SU, AU, and WI were 38.26, 143.46, 34.58, and 7.40 mm, respectively. The trend rates for these seasons were -0.13, -0.14, -0.51, and 0.05 mm·a-1, indicating a decreasing trend in all seasons except for WI, in which MAP showed an increasing trend. The most significant decrease was observed in AU. The spatial distribution of MAP in the Hami region exhibited an inverse pattern compared to that of *PET*, showing a high value in the central area and lower values in the surrounding regions (Figure 6a). The multiyear average MAT, Max-T, and Min-T were 7.33, 14.24, and 0.10 °C, respectively. The trend rates for each of these variables were 0.02, 0.03, and 0.01 °C·a-1 (Figure 5b–d), indicating an overall increasing trend in temperatures in the Hami region. The MAT, Max-T, and Min-T exhibited similar trends across all seasons. In SP, SU, and AU, there was an increasing trend with similar trend rates, while in WI, there was a decreasing trend with a consistent trend rate of -0.03 °C·a-1. The spatial distributions of MAT, Max-T, and Min-T were similar to that of *PET*, demonstrating a tendency toward lower values in the central area and higher values in the surrounding regions (Figure 6b–d).
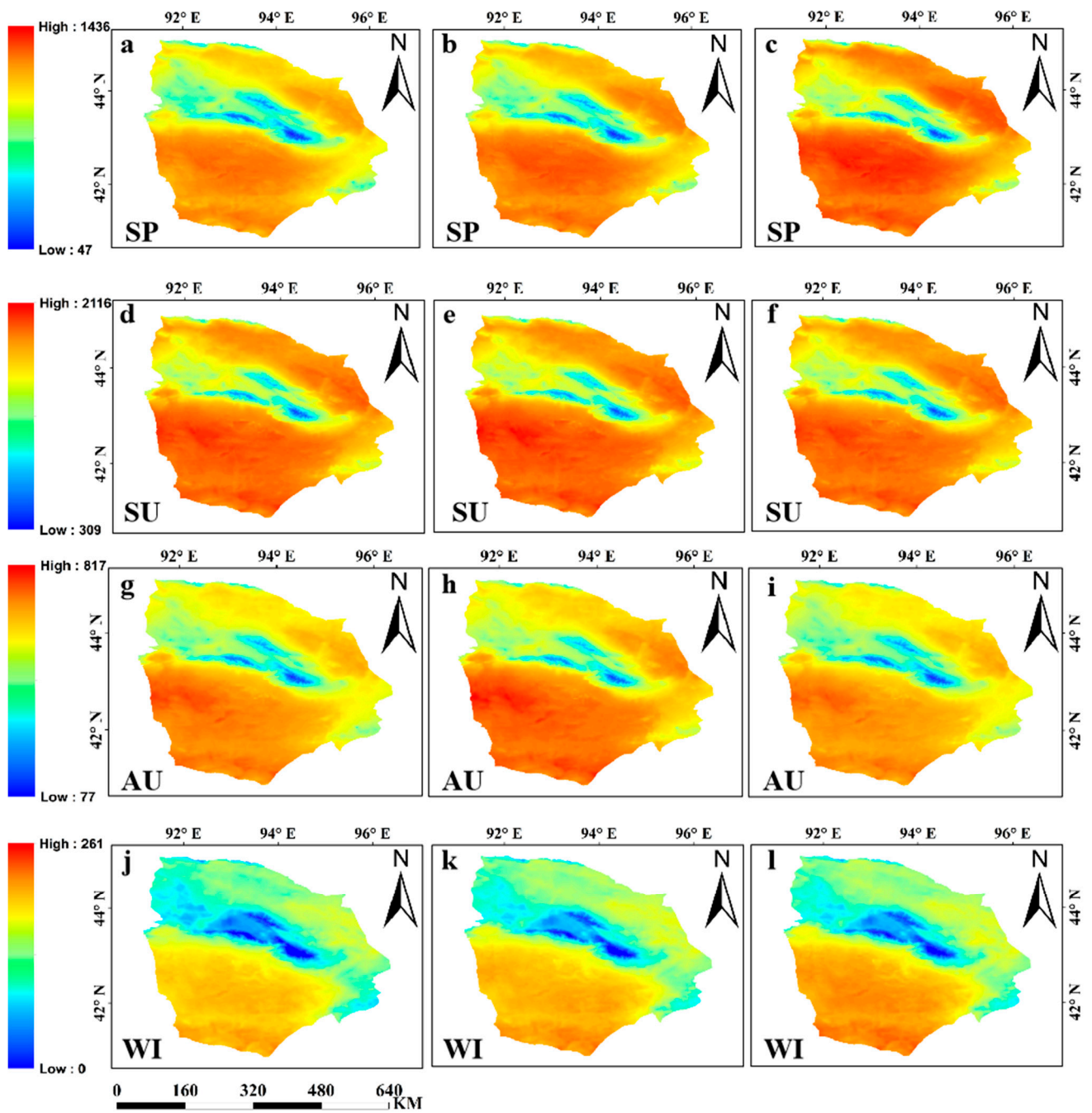
Figure 4. The spatiotemporal distribution (**a**–**l**) of *PET* during the four seasons of 1991, 2005, and 2020 in the Hami region is illustrated [(**a**,**d**,**g**,**j**): 1991; (**b**,**e**,**h**,**k**): 2005; (**c**,**f**,**i**,**l**): 2020].
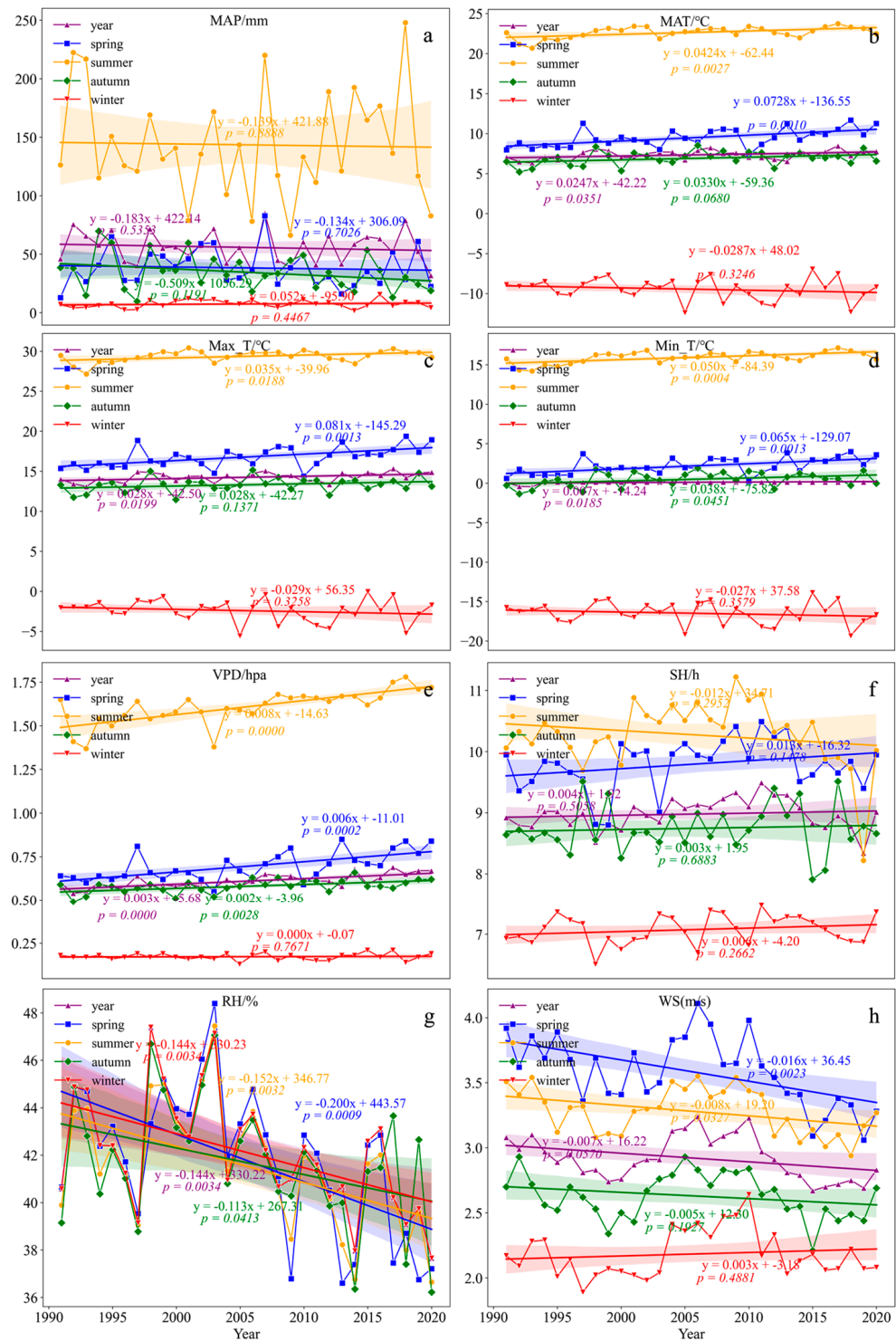
Figure 5. Interannual and seasonal variation trends of various environmental factors in Hami region [(**a**) average precipitation; (**b**) average temperature; (**c**) average maximum temperature; (**d**) average minimum temperature; (**e**) average vapor pressure deficit; (**f**) average sunshine hours; (**g**) average relative humidity; (**h**) average wind speed].
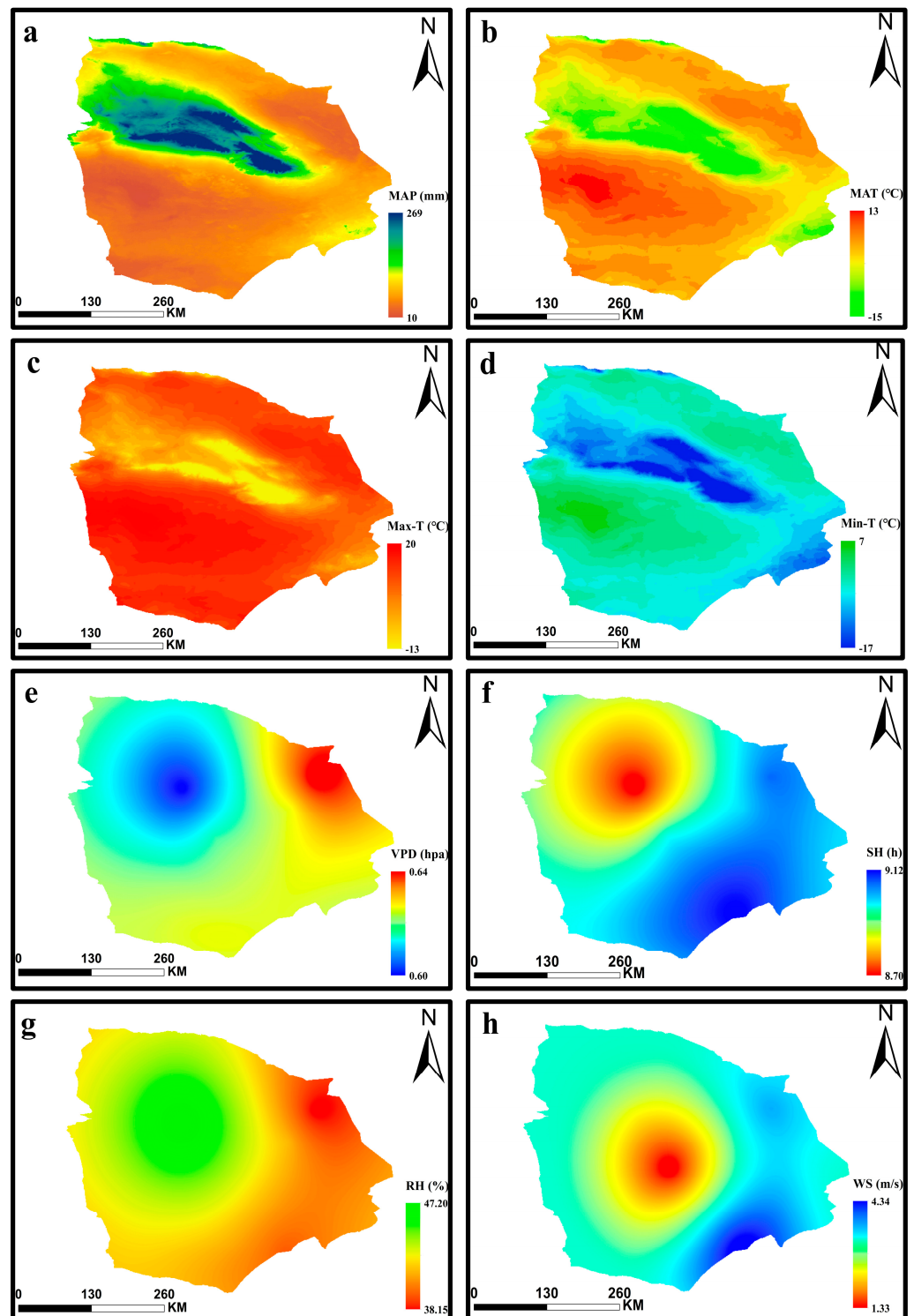
Figure 6. Spatial distribution of environmental factors in Hami region [(**a**) average precipitation; (**b**) average temperature; (**c**) average maximum temperature; (**d**) average minimum temperature; (**e**) average vapor pressure deficit; (**f**) average sunshine hours; (**g**) average relative humidity; (**h**) average wind speed].

The multiyear average VPD in the study area was 0.61 hpa, with a trend rate of 0.003 hpa·a-1 (Figure 5e). This indicates an overall increasing trend in VPD in the study area. The trend rates for VPD in SP, SU, AU, and WI were 0.006, 0.008, 0.002, and 0.000 hpa·a-1, respectively. This suggests that the VPD during WI showed the smallest change over the

time series, while the other seasons exhibited an increasing trend, with the most significant increase observed in SU. The spatial distribution was characterized by relatively high VPD in the northeastern region and relatively low values in the northwestern region (Figure 6e). The multiyear average SH in the study area was 8.98 h, with a trend rate of 0.004 h·a-1 (Figure 5f). This indicates an overall increasing trend in SH in the study area. The trend rates for SH in SP, SU, AN, and WI were 0.013, −0.012, 0.003, and 0.006 h·a-1, respectively. This suggests that only the SH in SU showed a decline over time, while the other seasons exhibited an increasing trend, with the most significant increase observed in SP. The overall spatial distribution shows a gradual decrease in SH from southeast to northwest (Figure 6f). The multiyear average RH in the study area was 42.11%, with a trend rate of −0.144%·a-1 (Figure 5g). This indicates an overall trend of drying in the study area. The trend rates for RH in SP, SU, AU, and WI were −0.20, −0.152, −0.113, and −0.114%·a-1, respectively. This suggests a decreasing trend in RH for each season, with the most significant decrease observed in SP. The spatial distribution showed a gradual increase in RH from southeast to northwest (Figure 6g). The multiyear average WS in the study area was 2.92 m·s-1, with a trend rate of −0.007 m·s-1·a-1 (Figure 5h). This indicates an overall decreasing trend in WS in the study area. The trend rates for WS in SP, SU, AU, and WI were −0.016, −0.008, −0.005, and 0.003 m·s-1·a-1, respectively. This suggests that only the average WS in WI was increasing, while the WS in other seasons was decreasing, with the most significant decrease observed in SP. The spatial distribution reveals a pattern of lower WS in the central area and higher WS in the surrounding regions, with the southeastern area experiencing the highest WS (Figure 6h).

3.2.2. Partial Correlation Analysis of *PET* and Various Climatic Factors in the Hami Region

ET is influenced by a combination of various environmental factors, primarily including temperature, WS, SH, RH, VPD, MAP, and other meteorological elements. There are numerous factors influencing the variation of *PET*, and these factors interact with each other. Therefore, the causes of changes in *PET* are highly complex. In order to explore the causes of the annual and seasonal variations in *PET* in the Hami region, eight meteorological factors (MAP, MAT, Max-T, Min-T, VPD, SH, WS, RH) were selected. The dominant factors influencing *PET* were studied using partial correlation analysis. Based on the partial correlation coefficients between *PET* and various climatic factors (Figure 7), the Max-T, Min-T, WS, and VPD (0.771, 0.314, 0.034, 0.114) showed a positive correlation with annual *PET*. An increase in these climatic factors led to an increase in *PET*. On the other hand, RH, MAP, SH, and MAT (−0.069, −0.191, −0.026, −0.145) exhibited a negative correlation with annual *PET*. An increase in these climatic factors resulted in a decrease in *PET*. Among these, the partial correlation coefficient of Max-T was 0.771, which made it the primary climatic factor influencing annual *PET*, reaching a significant level ($p < 0.01$). Different climatic factors had varying degrees of impact on *PET* in different seasons. In SP, the factors with significant influence on *PET* were WS (0.379), VPD (−0.379), and RH (−0.370). In SU, VPD (−0.330), SH (0.253), and RH (−0.333) played significant roles. In AU, MAP (−0.507) was a major influencing factor, while in WI, SH (−0.211), MAT (0.185), and Min-T (−0.183) had notable impacts.
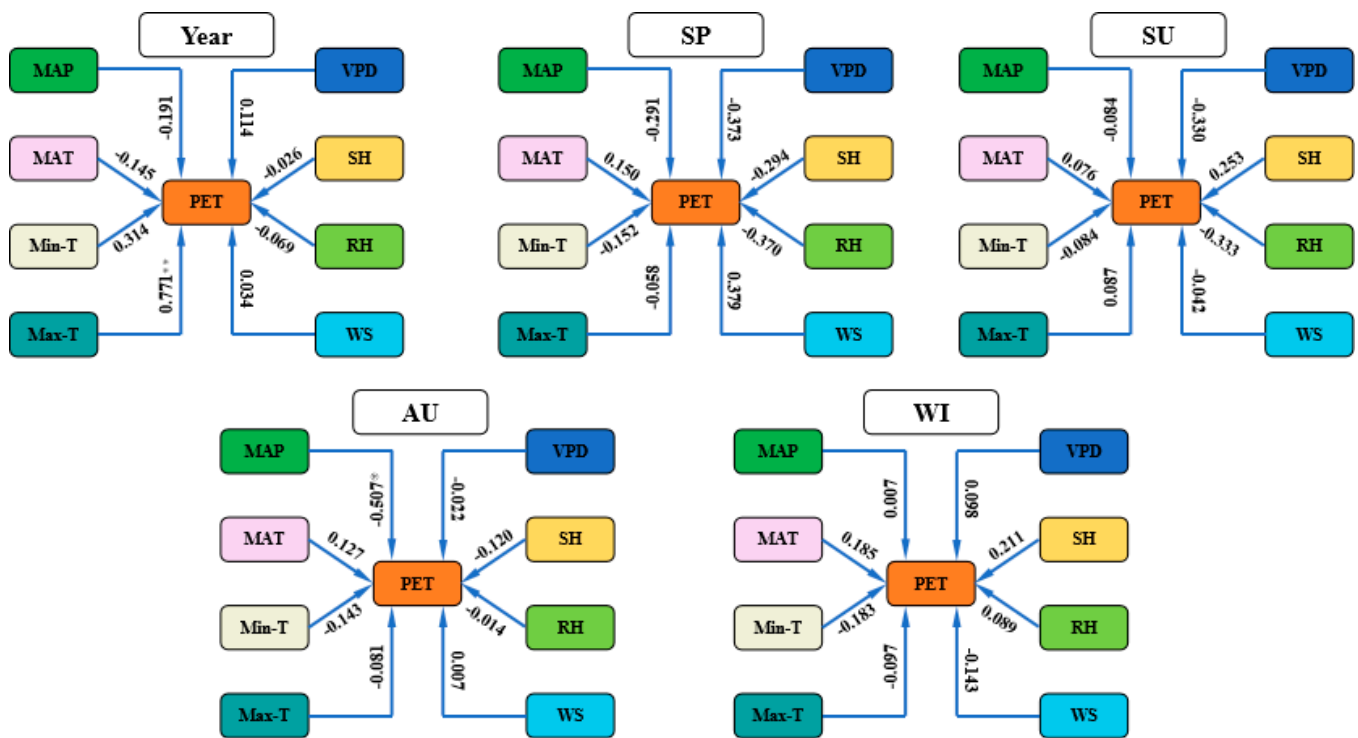
Figure 7. Partial correlation coefficients between annual and seasonal *PET* and environmental factors in the Hami region.

4. Discussion

Studying the temporal variations of *PET* contributes to understanding the trends in climate change; such research provides a predictive foundation for water resource management, guiding adaptation in fields such as agriculture and urban planning to cope with climate change [28]. In this study, the annual average *PET* in the Hami region from 1991 to 2020 was 871.54 mm; during WI, *PET* showed a decreasing trend, while in other seasons and annually, *PET* exhibited an increasing trend. Related studies showed that *PET* increased significantly in the arid areas of Northwest China [29–31]. The findings of the current study are generally consistent with this conclusion, with the only difference being that the winter *PET* in the Hami region showed a decreasing trend, which may be due to the drop in WI temperature; the specific reasons will be further studied.

Studying the spatial distribution pattern of potential evaporation is helpful in formulating differentiated water resource management strategies for various regions. This contributes to improving irrigation efficiency, ensuring the sustainability of agricultural and urban water usage [32]. The present study indicates that the annual and seasonal *PET* in the Hami region generally followed a distribution pattern of lower values in the central part and higher values in the surrounding areas. The southern region exhibited the highest *PET*, while the northwestern region experienced relatively lower values. Metzger et al. and other researchers have found that in desert ecosystems, *ET* is strongly influenced by vegetation and land use [33]. From homogeneous shrub areas to heterogeneous open forests and ranging further to sparsely covered arid agricultural lands, *ET* continuously increases. The central region of the Hami area is primarily characterized by natural grassland and orchards with a certain degree of coverage, resulting in relatively low *ET*. In contrast, the surrounding areas consist mainly of bare land and desert, which lack coverage, leading to relatively high *ET*. This observation aligns closely with the conclusions drawn by Metzger et al.

Clear identification of the driving factors influencing *PET* is crucial for understanding the impacts of meteorology, land use, and climate change on the water cycle. This knowledge contributes to more accurate predictions of *PET* changes, providing scientific

guidance for irrigation, water resource management, and ecological conservation [34–36]. Research findings indicate that Max-T has a partial correlation coefficient of 0.771 with *PET*, making it the primary factor influencing annual *PET* changes in the Hami region. The partial correlation coefficient for MAP is −0.507, signifying it as the main factor influencing autumn *PET* changes. The factors of MAT, Min-T, WS, VPD, SH, and RH play enhancing or diminishing roles in the annual and seasonal variations of *PET* but do not reach statistical significance. Yao et al. found that solar radiation is the primary factor influencing *PET* in most parts of China, while WS is the predominant factor affecting *PET* in the Northwest region of China [31]. The results of our study differ from this conclusion, possibly because we did not include solar radiation data in our research. Solar radiation plays a crucial role as the primary energy driver in the Earth's climate system. When solar radiation reaches the Earth's surface, it directly influences the maximum temperature, consequently impacting the *PET*. Gao et al. conducted a study on the spatiotemporal variation of *ET* in 580 locations across China. Through partial correlation analysis, they found that SH, WS, and RH significantly influence *ET* [29]. From this, it can be inferred that the variations in *ET* across different regions result from the combined effects of multiple key climatic factors. Although WS is a primary climatic factor influencing *PET* on a large scale in the northwestern region, for localized small-scale areas within the western region, changes in underlying surface characteristics, such as determining canopy resistance, soil surface resistance, and other factors, also significantly affect *PET* [37,38]. Consequently, the dominant climatic factors affecting *PET* can change within localized areas due to these underlying surface features. However, its limitation lies in the lack of in-depth research on the impact of local land-use changes on *PET*. This is an area where the study falls short, and future research should delve more into factors such as land-use changes for a comprehensive understanding.

5. Conclusions

This study analyzed the spatiotemporal variations of *PET* in the Hami region of Xinjiang over the past 30 years. It expanded beyond the limitations of estimating *PET* at a single point and filled a gap in the existing research on regional changes in *PET* and their impact. The results can provide a scientific basis for water resource management strategies in arid regions. The conclusions drawn are as follows:

(1) In the hyper-arid Hami region in Northwest China, the annual *PET* showed a fluctuating increasing trend from 1991 to 2020. The interannual trends of *PET* for full years, SP, SU, AU, and WI were 0.933, 2.744, 0.906, 0.488, and −0.406 mm·a-1, respectively. This indicates that, except for WI, *PET* increased in each season as well as annually, with the largest growth rate in SP. Spatial variations in the interannual changes of *PET* were observed across different seasons in the region.

(2) In the Hami region, the multiyear annual average *PET* ranged between 113 and 1111 mm from 1991 to 2020. The *PET* ranges for SP, SU, AU, and WI were 47–1436, 309–2116, 77–817, and 0–261 mm, respectively. The distribution of *PET* for different years and seasons across the entire region exhibited a consistent pattern, characterized by lower values in the central area and higher values in the surrounding regions. The southern area had the highest *PET*, while the northwestern region had relatively lower values.

(3) The impact of trends and magnitudes of meteorological factors on annual and seasonal potential evapotranspiration varies. The dominant factor influencing annual *PET* is Max-T, while for AU *PET*, the main influencing factor is MAP. Other factors play a role in enhancing or reducing the changes in annual *PET*.

Author Contributions: Y.L.: conceptualization, draft syllabus, investigation, data collation and validation, visualization and interpretation, analysis, write-up, and proofreading; Y.Y.: conceptualization, analysis, data interpretation, write-up, review, and editing; L.D., L.S., Z.G., J.Z., C.L. and J.H.: conceptualization and collection of primary data; E.Ł., I.M. and M.W.: provision of paper-writing suggestions. All authors have read and agreed to the published version of the manuscript.

Institutional Review Board Statement: Not applicable.

Informed Consent Statement: Statement not applicable.

Data Availability Statement: The data presented in this study are available on request from the lead author. The data are not publicly available because they also form part of an ongoing study.

Conflicts of Interest: The authors declare no conflicts of interest.

References

1. Liu, B.; Henderson, M.; Zhang, Y.; Ming, X. Spatiotemporal change in China's climatic growing season: 1955–2000. *Clim. Chang.* **2010**, *99*, 93–118. [CrossRef]
2. Hajimirzajan, A.; Vahdat, M.; Sadegheih, A.; Shadkam, E.; Bilali, H.E. An integrated strategic framework for large-scale crop planning: Sustainable climate-smart crop planning and agri-food supply chain management. *Sustain. Prod. Consum.* **2020**, *26*, 709–732. [CrossRef]
3. Vicente-Serrano, S.M.; Azorin-Molina, C.; Sanchez-Lorenzo, A.; Revuelto, J. Sensitivity of reference evapo-transpiration to changes in meteorological parameters in Spain (1961–2011). *Water Resour Res.* **2014**, *50*, 8458–8480. [CrossRef]
4. Bond, N.A.; Bumbaco, K.A. Summertime potential evapotranspiration in eastern Washington state. *J. Appl. Meteorol. Climatol.* **2015**, *54*, 1090–1101. [CrossRef]
5. Liu, L.; Zhang, Z.Y.; Yan, Q. Spatiotemporal Changes of Potential Evaporation of the Northern Slope in Tianshan Mountains. *Res. Soil Water Conserv.* **2015**, *22*, 306–311.
6. Wells, N.; Goddard, S.; Hayes, M.J. A Self-Calibrating Palmer Drought Severity Index. *J. Clim.* **2004**, *17*, 2335–2351. [CrossRef]
7. Kimura, R. Global detection of aridification or increasing wetness in arid regions from 2001 to 2013. *Nat. Hazards* **2020**, *103*, 2261–2276. [CrossRef]
8. McCabe, G.J.; Hay, L.E.; Bock, A.; Markstrom, S.L.; Atkinson, R.D. Inter-annual and spatial variability of Hamon potential evapotranspiration model coefficients. *J. Hydrol.* **2015**, *521*, 389–394. [CrossRef]
9. Bai, P.; Liu, X.; Yang, T.; Li, F.; Liang, K.; Hu, S.; Liu, C. Assessment of the Influences of Different Potential Evapotranspiration Inputs on the Performance of Monthly Hydrological Models under Different Climatic Conditions. *J. Hydrometeorol.* **2016**, *17*, 2259–2274. [CrossRef]
10. Ma, T.X.; Liang, Y.; Lau, M.K.; Liu, B.; Wu, M.M.; He, H.S. Quantifying the relative importance of potential evapotranspiration and timescale selection in assessing extreme drought frequency in conterminous China. *Atmos. Res.* **2021**, *263*, 105797. [CrossRef]
11. Ferreira, L.B.; da Cunha, F.F.; de Oliveira, R.A.; Filho, E.I.F. Estimation of reference evapotranspiration in Brazil with limited meteorological data using ANN and SVM—A new approach. *J. Hydrol.* **2019**, *572*, 556–570. [CrossRef]
12. Valipour, M.; Gholami Sefidkouhi, M.A.; Raeini−Sarjaz, M. Selecting the best model to estimate potential evapotranspiration with respect to climate change and magnitudes of extreme events. *Agric. Water Manag.* **2017**, *180*, 50–60. [CrossRef]
13. McMahon, T.A.; Peel, M.C.; Lowe, L.; Srikanthan, R.; McVicar, T.R. Estimating actual, potential, reference crop and pan evaporation using standard meteorological data: A pragmatic synthesis. *Hydrol. Earth Syst. Sci.* **2013**, *17*, 1331–1363. [CrossRef]
14. Sonali, P.; Nagesh Kumar, D. Spatio-temporal variability of temperature and potential evapotranspiration over India. *J. Water Clim. Chang.* **2016**, *7*, 810–822. [CrossRef]
15. Penman, H.L. Natural evaporation from open water, bare soil and grass. *Proc. R. Soc. Lond. A* **1948**, *193*, 120–146.
16. Gan, G.; Liu, Y.; Sun, G. Understanding interactions among climate, water, and vegetation with the Budyko framework. *Earth-Sci Rev.* **2021**, *212*, 103451. [CrossRef]
17. Gedney, N.; Cox, P.M.; Betts, R.A.; Boucher, O.; Huntingford, C.; Stott, P.A. Detection of a direct carbon dioxide effect in continental river runoff records. *Nature* **2006**, *439*, 835–838. [CrossRef] [PubMed]
18. Zhang, Q.; Qi, T.Y.; Li, J.F.; Singh, V.P.; Wang, Z.Z. Spatiotemporal variations of pan evaporation in China during 1960–2005: Changing patterns and causes. *Int. J. Climatol.* **2015**, *35*, 903–912. [CrossRef]
19. Yin, Y.H.; Wu, S.H.; Dai, E.F. Determining factors in potential evapotranspiration changes over China in the period 1971–2008. Chin. *Sci. Bull.* **2010**, *55*, 3329–3337. [CrossRef]
20. Zhang, Y.; Liu, C.; Tang, Y.; Yang, Y. Trends in Pan Evaporation and Reference and Actual Evapotranspiration across the Tibetan Plateau. *J. Geophys. Res. Atmos.* **2007**, *112*. [CrossRef]
21. Gao, G.; Chen, D.; Xu, C.Y.; Simelton, E. Trend of estimated actual evapotranspiration over China during 1960–2002. *J. Geophys. Res.* **2007**, *112*, D11120. [CrossRef]
22. Peterson, T.C.; Golubev, V.S.; Groisman, P.Y. Evaporation losing its strength. *Nature* **1995**, *377*, 687–688. [CrossRef]
23. Jhajharia, D.; Dinpashoh, Y.; Kahya, E.; Singh, V.P.; Fakheri-Fard, A. Trends in reference evapotranspiration in the humid region of northeast India. *Hydrol. Process.* **2012**, *26*, 421–435. [CrossRef]

24. Burn, D.H.; Hesch, N.M. Trends in evaporation for the Canadian Prairies. *J. Hydrol.* **2007**, *336*, 61–73. [CrossRef]

25. Roderick, M.L.; Rotstayn, L.D.; Farquhar, G.D.; Hobbins, M.T. On the attribution of changing pan evaporation. *Geophys. Res. Lett.* **2007**, *34*, L17403. [CrossRef]

26. Fisher, J.B.; Melton, F.; Middleton, E.; Hain, C.; Anderson, M.; Allen, R.; McCabe, M.F.; Hook, S.; Baldocchi, D.; Townsend, P.A. The Future of Evapotranspiration: Global Requirements for Ecosystem Functioning, Carbon and Climate Feedbacks, Agricultural Management, and Water Resources. *Water Resour. Res.* **2017**, *53*, 2618–2626. [CrossRef]

27. Fu, Y.P.; Xin, S.; Wang, Y.; Cao, Z.L. Adaptability Analysis of Three Spatial Interpolation Methods in Temperature—A Case Study of Jiangxi Province. *J. Green Sci. Technol.* **2023**, *25*, 51–56.

28. Rehana, S.; Monish, N.T. Impact of potential and actual evapotranspiration on drought phenomena over water and energy-limited regions. *Theor. Appl. Climatol.* **2021**, *144*, 215–238. [CrossRef]

29. Gao, G.; Chen, D.; Ren, G.; Chen, Y.; Liao, Y. Spatial and temporal variations and controlling factors of potential evapotranspiration in China: 1956–2000. *J. Geogr. Sci.* **2006**, *16*, 3–12. [CrossRef]

30. Thomas, A. Spatial and temporal characteristics of potential evapotranspiration trends over China. *Int. J. Climatol.* **2000**, *20*, 381–396. [CrossRef]

31. Yao, Y.; Zhao, S.; Zhang, Y.; Jia, K.; Liu, M. Spatial and Decadal Variations in Potential Evapotranspiration of China Based on Reanalysis Datasets during 1982–2010. *Atmosphere* **2014**, *5*, 737–754. [CrossRef]

32. Sun, S.; Wang, G.; Huang, J.; Mu, M.; Yan, G.; Liu, C.; Hua, W. Spatial pattern of reference evapotranspiration change and its temporal evolution over Southwest China. *Theor. Appl. Climatol.* **2016**, *130*, 979–992. [CrossRef]

33. Metzger, J.C.; Landschreiber, L.; Gröngröft, A.; Eschenbach, A. Soil evaporation under different types of land use in southern African savanna ecosystems. *J. Plant Nutr. Soil Sci.* **2014**, *177*, 468–475. [CrossRef]

34. Shi, H.; Li, T.; Wang, G. Temporal and spatial variations of potential evaporation and the driving mechanism over Tibet during 1961–2001. *Hydrol. Sci. J.* **2017**, *62*, 1469–1482. [CrossRef]

35. Li, Z.X.; Feng, Q.; Wei, L.; Wang, T.T.; Gao, Y.; Wang, Y.M.; Cheng, A.F.; Li, J.G.; Liu, L. Spatial and temporal trend of potential evapotranspiration and related driving forces in Southwestern China, during 1961–2009. *Quat. Int.* **2014**, *336*, 127–144.

36. Luo, K.; Tao, F.; Deng, X.; Moiwo, J.P. Changes in potential evapotranspiration and surface runoff in 1981–2010 and the driving factors in Upper Heihe River Basin in Northwest China. *Hydrol. Process.* **2016**, *31*, 90–103. [CrossRef]

37. Brauman, K.A.; Freyberg, D.L.; Daily, G.C. Potential evapotranspiration from forest and pasture in the tropics: A case study in Kona, Hawai'i. *J. Hydrol.* **2012**, *440–441*, 52–61. [CrossRef]

38. Katerji, N.; Rana, G. Crop reference evapotranspiration: A discussion of the concept, analysis of the process and validation. *Water Resour Manag.* **2011**, *25*, 1581–1600. [CrossRef]